# Coherent Control Protocol for Separating Energy-Transfer Pathways in Photosynthetic Complexes by Chiral Multidimensional Signals[†]

Dmitri V. Voronine,*,[‡] Darius Abramavicius,[§] and Shaul Mukamel

Department of Chemistry, University of California, Irvine, California

ABSTRACT: Adaptive optimizations performed using a genetic algorithm are employed to construct optimal laser pulse configurations that separate spectroscopic features associated with the two main energy-transfer pathways in the third-order nonlinear optical response simulated for the Fenna—Matthews—Olson (FMO) photosynthetic complex from the green sulfur bacterium *Chlorobium tepidum*. Superpositions of chirality-induced tensor components in both collinear and noncollinear pulse configurations are analyzed. The optimal signals obtained by manipulating the ratios of various 2D spectral peaks reveal detailed information about the excitation dynamics.
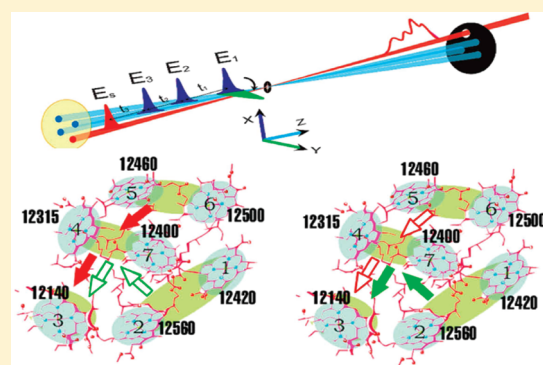
1. INTRODUCTION

Coherent multidimensional nonlinear optical spectroscopy has been widely used for the investigation of ultrafast vibrational and electronic processes in a variety of molecular and semiconductor systems.[1−6] Multidimensional spectra contain rich information about coherent and dissipative dynamics in molecular aggregates. The complexity of the spectra may be reduced by suppressing selected features by making use of interference of Liouville space pathways in the nonlinear response.[3] Recent developments include the design of optimal laser pulse sequences with a goal of achieving a higher spectral resolution and improved structural sensitivity on an ultrafast time scale, in analogy with a multidimensional NMR.[7,8]

Among the most exciting developments in multidimensional electronic spectroscopy is the discovery of the long-lived electronic quantum coherence in pigment—protein light-harvesting complexes from photosynthetic bacteria at 77 K[9] and from bacteria[10] and marine algae[11] at ambient temperature. Theoretical analysis has allowed us to distinguish between classical and quantum transport.[12] The analysis is, however, limited by the ability to resolve weak spectral peaks from congested manifolds of states. New experimental techniques that overcome these difficulties may shed light on the detailed mechanism of photosynthesis.

Chirality-induced (CI) multidimensional optical spectroscopy has been recently proposed and predicted to provide a higher spectral resolution than its conventional nonchiral counterpart.[5,6] It has been applied to resolve weak spectral features in peptides and in light-harvesting complexes.[13−17] In our earlier work, we demonstrated how various laser pulse configurations may be designed to separate coherent dynamics from dissipative energy relaxation.[18] CI signals show a richer 2D peak pattern and enhance the differences between the spectra from two species of the photosynthetic bacteria.[19]

The full power of CI multidimensional spectroscopy may be realized by active manipulation of pulses using coherent control techniques.[16] Numerous laser pulse parameters such as wave vectors, polarizations, phases, and amplitudes may be used as "control knobs". Chirality-sensitive delicate spectral features of various physical, chemical, and biological processes may then be investigated and optimized. Coherently controlled multidimensional spectroscopy performed with shaped laser pulses has been investigated both theoretically[20−22] and experimentally.[23] Optimal laser pulses were found in adaptive optimizations. Shaped laser pulses may also be used to control excitation dynamics and modify the response of molecular aggregates. Coherent control of molecular processes by laser pulse shaping has been applied.[24,25] The control of energy transfer in light-harvesting complexes was demonstrated.[26,27]

Laser pulse polarizations constitute some of the simplest control knobs. Optimal pulse polarization configurations for the control of multidimensional spectral features have recently been proposed[18] and implemented experimentally.[28−30] Polarization control was applied to investigate the dynamics of peptides.[31,32] Pulse polarization configurations that suppress diagonal peaks and resolve and enhance cross peaks were proposed. Adaptive optimizations with a genetic algorithm were used to design optimal pulse configurations in simulated nonchiral spectra of amyloid fibrils[33] and in CI spectra of a porphyrin dimer.[16] High degree of control was demonstrated by adaptive control of the
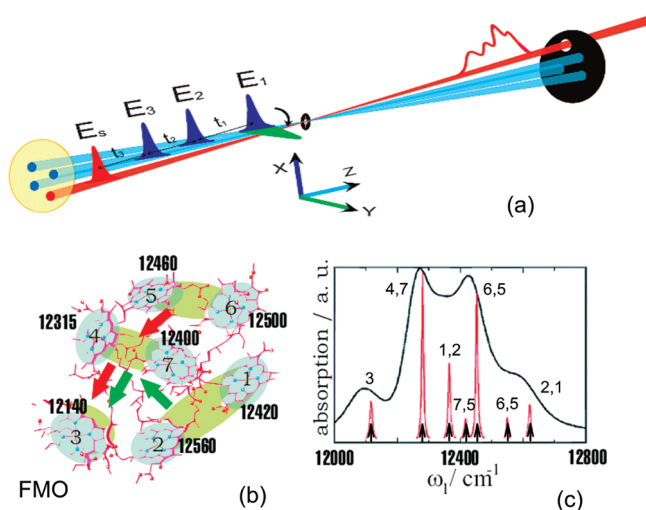
Figure 1. (a) Coherent multidimensional third-order spectroscopy in a noncollinear configuration. Three laser pulses with variable wave vector directions, time delays, and polarizations generate a nonlinear optical signal field. (b) Arrangement of the Bacteriochlorophyll *a* molecules in the FMO complex from the photosynthetic green sulfur bacterium *Chlorobium tepidum*. The red and green arrows mark the fast and slow energy-transfer pathways, respectively. The molecules are numbered 1 through 7. The molecular site energies which are different due to their different protein environments are shown in (b). The seven delocalized single exciton energies are shown as narrow lines (arrows) in the linear absorption spectrum in (c). The individual molecules that contribute strongly to each state are indicated. The spectrum simulated at 77 K matches the experiments of Brixner et al.[35]

chiral response. The initial success of these investigations inspired further applications aimed at overcoming spectral congestion and enhancing weak multidimensional signals.

In this work, we simulate polarization-controlled CI multidimensional spectroscopy of the Fenna–Matthews–Olson (FMO) complex from the photosynthetic green sulfur bacterium *Chlorobium tepidum*.[34] Improved resolution and sensitivity are demonstrated. Molecular movies may be obtained by displaying the optimized signals at different times. As was done in ref 16, we use a genetic algorithm to perform adaptive optimizations of a linear combination of the third-order CI tensor components to isolate multidimensional spectral features due to two energy-transfer pathways in the FMO complex. Simulation details and model system parameters are described in section 2. The results are presented in sections 3 and 4 and discussed in section 5.

2. SIMULATION PROTOCOL AND MODEL SYSTEM

2.1. CI Coherent Multidimensional Nonlinear Optical Spectroscopy.

The coherent multidimensional third-order nonlinear optical spectroscopy setup involves four laser pulses, as shown in Figure 1a. We consider the photon echo signal generated in the direction $k_S = -k_1 + k_2 + k_3$, where k_i ($i = 1, 2, 3$) and k_S are the wave vectors of the incident and the signal pulses, respectively. The forth (local oscillator) pulse E_S is used for heterodyne detection of the signal electric field. Multidimensional signals are generated by scanning the three time delays between pulses and performing a Fourier transform with respect to these delays. The pulse wave vectors may be arranged in a noncollinear configuration to select the desired k_S signal.

Alternatively, this can be achieved in a collinear configuration using phase cycling.

By varying pulse polarizations, we can select various tensor components of the response. The three nonchiral linearly independent third-order tensor components in the dipole approximation are $\nu_4\nu_3\nu_2\nu_1 = xxyy$, $xyxy$, and $xyyx$, where ν_i is the polarization direction of the *i*th laser pulse. The all-parallel nonlinear signal is a sum of these three tensor components, $xxxx = xxyy + xyxy + xyyx$. In addition there are nine linearly independent CI third-order tensor components.[13−15] They are denoted $T_j^{(cl/ncl)} = \mathcal{R}_{\nu_4\nu_3\nu_2\nu_1}(\kappa_4\kappa_3\kappa_2\kappa_1)$ with $j = 1, ..., 9$, with wave vector directions κ_i ($i = 1, 2, 3, S$). Three $T_3^{(cl)}$, $T_6^{(cl)}$, and $T_8^{(cl)}$ are collinear, and the other six tensor components are noncollinear. The nine linearly independent CI third-order tensor components are $T_1^{(ncl)} = \mathcal{R}_{xyzx}(z,x,-x,-z)$, $T_2^{(ncl)} = \mathcal{R}_{xyxz}(z,x,z,x)$, $T_3^{(cl)} = \mathcal{R}_{xyxx}(z,z,z,z)$, $T_4^{(ncl)} = \mathcal{R}_{xyxx}(z,z,y,y)$, $T_5^{(ncl)} = \mathcal{R}_{xxyz}(z,z,x,x)$, $T_6^{(cl)} = \mathcal{R}_{xxyx}(z,z,z,z)$, $T_7^{(ncl)} = \mathcal{R}_{xxyx}(z,y,z,y)$, $T_8^{(cl)} = \mathcal{R}_{xxxy}(z,z,z,z)$, and $T_9^{(ncl)} = \mathcal{R}_{xxxy}(z,y,-y,-z)$. These signals scale linearly with the wave vectors (in contrast to the dipole approximation where the signals are independent of wave vectors) and change sign upon parity transformation. These nonlinear analogues of circular dichroism are induced by the system's chirality and often provide a higher spectral resolution due to interferences between contributions of different signs.

We have constructed the linear combination of the nine tensor components

$$S^{(CI)} = \sum_{j=1}^{9} c_j T_j^{(cl/ncl)} \quad (2.1)$$

and optimized the complex coefficients $c_j = c_j' + ic_j''$ using a genetic algorithm in order to highlight specific weak cross peaks. The 18-parameter search space is reduced to 6 in the collinear case. Details of the genetic algorithm were described previously.[16,36] Convergence was typically achieved in several hundred generations.

2.2. Energy Transfer Pathways in the FMO Complex of Photosynthetic Bacterium *Chlorobium tepidum*.

FMO is the first photosynthetic complex for which the atomic resolution crystal structure was obtained.[37] In nature FMO serves as a mediator of energy transfer from giant light-absorbing antennae, called chlorosomes, to a reaction center. It is a trimer in which each unit consists of eight Bacteriochlorophyll (BChl) *a* molecules arranged in a chiral configuration and surrounded by a protein bath (Figure 1b). The heterogeneous bath shifts the various site energies. These are given (in cm^{-1}) in Figure 1b. Seven of the BChl *a* molecules are coupled and form single- and double-exciton manifolds with 7 and 21 excited states, respectively. The single-exciton states are nondegenerate and delocalized over several (2−3) molecules. The main contributing molecules to each single-exciton state are marked in the linear absorption spectrum in Figure 1c. The lowest-energy state is localized on the BChl *a* molecule 3. Previous measurements and simulations revealed the two main, fast and slow, energy-transfer pathways, which transfer energy to the lowest-energy BChl *a* molecule 3, marked by the red and green arrows in Figure 1b, respectively. Excitons 1 and 2 are shared by these pathways. Excitons 3 and 7 contribute exclusively to the slow pathway, while excitons 4, 5, and 6 contribute to the fast.

The structural and bath parameters of the Hamiltonian were given previously.[18] Briefly, we used an isotropic sample of FMO complexes described by a Hamiltonian developed by Aartsma and modified by Fleming and co-workers[35] with a Brownian
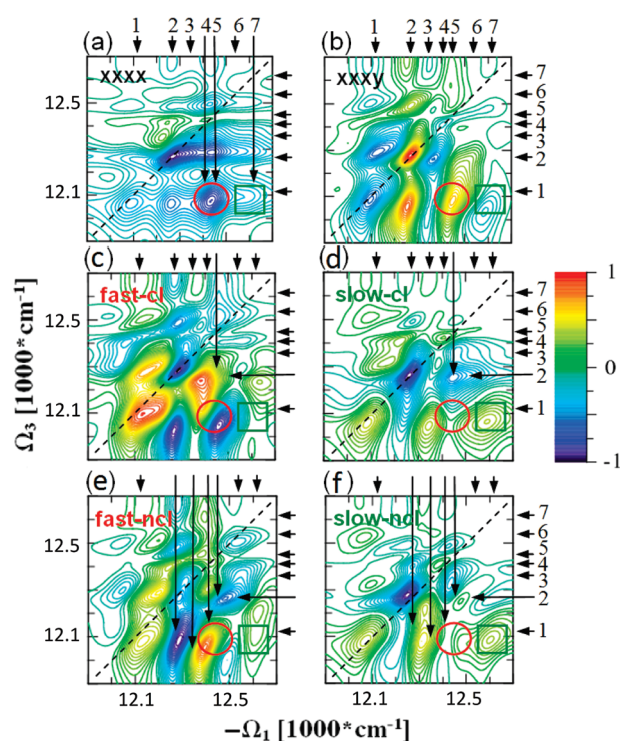
Figure 2. 2D spectra of FMO at t_2 = 5 ps: (a) imaginary (absorptive) part of the nonchiral *xxxx* signal; (b) real (absorptive) part of the CI *xxxy* signal; (c,d) CI collinear optimal coherently controlled linear combinations for the fast and slow energy-transfer pathways, respectively (real parts); (e,f) corresponding optimal noncollinear signals. The arrows and numbers indicate single-exciton states and facilitate peak assignments. A red circle and a green square highlight cross peaks used for the optimization of the fast and slow energy-transfer pathways, respectively.

Table 1. Optimal Coefficients $c_j = c_j' + ic_j''$ from the Optimal Linear Combinations of the CI 2D Spectra of FMO for t_2 = 5 ps[a]

2D CI signal	fast−ncl	slow−ncl	fast−cl	slow−cl
$T_1^{(ncl)}$	−0.09 − 0.02i	0.33 − 0.35i	0	0
$T_2^{(ncl)}$	0.01 + 0.13i	0.23 − 0.04i	0	0
$T_3^{(cl)}$	0.23 + 0.13i	−0.08 + 0.13i	0.18 + 0.00i	−0.14 + 0.25i
$T_4^{(ncl)}$	−0.22 + 0.02i	0.21 + 0.08i	0	0
$T_5^{(ncl)}$	0.18 + 0.20i	−0.18 − 0.03i	0	0
$T_6^{(cl)}$	**−0.68 − 0.18i**	0.32 + 0.00i	−0.01 + 0.41i	**0.10 + 0.94i**
$T_7^{(ncl)}$	0.01 + 0.07i	**−0.14 + 0.54i**	0	0
$T_8^{(cl)}$	0.30 + 0.25i	−0.33 − 0.01i	**0.70 − 0.56i**	0.00 + 0.08i
$T_9^{(ncl)}$	−0.03 − 0.37i	0.27 − 0.08i	0	0

[a] Four optimizations are shown that disentangle the fast and slow energy-tranfer pathways using collinear (cl) and noncollinear (ncl) pulse configurations. The dominant tensor component in each optimization is given in bold.

oscillator bath at 77 K. These parameters were used to fit the experimental *xxxx* 2D spectra at various t_2 delay times.[35,38] Despite the success of the nonchiral *xxxx* 2D spectroscopy in determining the pathways, not all spectral features were clearly resolved. To resolve all of the energy-transfer steps and obtain a complete picture of the microscopic response, we simulate coherent control of multidimensional spectral features using adaptive optimization of a linear combination of response function tensor components in both collinear and noncollinear pulse configurations.

Different CI tensor components show characteristic peak patterns that reflect the variations of the spatial delocalization of different exciton states. All tensor components contain a mixture of spectral features due to both energy-transfer pathways in FMO. Our goal is to suppress spectral features of all other competing processes by controlling a coherent superposition of tensor components.

3. CONTROL OF CHIRAL 2D SIGNALS AT T_2 = 5 ps

We first constructed a superposition of the three CI collinear third-order tensor components. Our target is to resolve the two energy-transfer pathways in FMO that were recently revealed by 2D electronic spectroscopy.[35] We chose the ratio of two cross peaks at the waiting delay time t_2 = 5 ps as a control target. These cross peaks result from the energy transfer and grow with t_2, reaching a maximum at a long time. At t_2 = 5 ps, all coherences

have decayed, and only dissipative dynamics is observed in the 2D spectra. The selected cross peaks marked in Figure 2 result from the fast (red circle) and slow (green square) energy-transfer pathways. (Ω_1 and Ω_3 are the Fourier transform conjugate variables of the time delays t_1 and t_3, respectively.) Arrows with labels from 1 to 7 mark the corresponding single-exciton state energies. The selected cross peak of the fast energy-transfer pathway (red circle) is due to the decay of the two overlapping exciton states 4 and 5 to exciton 1 and will be labeled (4/5,1). The second cross peak (green square) is due to exciton 7 relaxing to exciton 1 and will be labeled (7,1).

The two cross peaks have the same sign (and color, blue) in the nonchiral *xxxx* 2D signal (Figure 2a). Broad line shapes limit the resolution. (7,1) appears as a shoulder and is not well resolved. In addition, (6,1), which is due to the fast pathway, has the same sign and further reduces the resolution of (7,1). The splitting of the two exciton states 4 and 5 is smaller than their line widths, and they are not resolved. Two-dimensional CI (2D CI) collinear signals are better resolved. The $T_8^{(cl)}$ 2D CI tensor component (*xxxy*) at t_2 = 5 ps is shown in Figure 2b. Diagonal and cross peaks due to various exciton states have different signs, depending on the exciton chirality. This provides a higher spectral resolution compared to that of the nonchiral signals. The shoulder of (7,1) in *xxxx* turns into a clearly resolved peak in *xxxy*. Cross peaks (4/5,1) and (7,1) have different signs in *xxxy* as they involve states which are delocalized over different molecules, resulting in excitons with an opposite sense of chirality. A new cross peak (3,1), which has not been resolved in nonchiral experimental signals, is now seen (blue peak).

To maximize spectral features due to the fast energy-transfer pathway, we maximize the ratio of the integrated cross peaks (4/5,1) and (7,1). The slow pathway is obtained by minimizing this ratio. Each peak intensity is obtained by integration square area ≈ $(100 \text{ cm}^{-1})^2$. The results are shown in Figure 2. The real part of the collinear 2D CI signals optimized to resolve the fast and slow energy-transfer pathways is shown in Figure 2c and d, respectively. Both optimizations were performed by combining the three CI tensor components $T_3^{(cl)}$, $T_6^{(cl)}$, and $T_8^{(cl)}$. We investigate how much control can be achieved by using this limited parameter space. Both optimizations achieved our goal of suppressing the undesired cross peaks. However, the peak resolution is not sufficient to distinguish the participating exciton state energies.

The optimal coefficients c_j are given in Table 1. They correspond to the four optimizations that disentangle the fast and slow energy-tranfer pathways. The dominant tensor components in each optimization are highlighted in bold. The sum of the modulus squares of all nine coefficients is normalized to unity.

We have next constructed a full noncollinear pulse configuration which combines all nine CI tensor components. We now have an 18-parameter space. The results of the optimized fast and slow pathways are shown in Figure 2e and f, respectively. The undesired cross peaks were suppressed. Other cross peaks belonging to the undesired pathway are also suppressed in both optimizations. For example, cross peak (7,1) is amplified, and (4/5,1) is suppressed in the slow pathway noncollinear (slow–ncl) optimization in Figure 2f. In addition, cross peak (3,1) of the slow pathway is resolved and maximized. Other peaks associated with the slow pathway are also optimized. For example, (5,2) is suppressed due to the low contribution of excitons 5 and 2 to the slow pathway. However, this peak is enhanced in the fast pathway noncollinear (fast–ncl) optimization in Figure 2e (see arrows).

Overall, the peak patterns in the collinear and noncollinear optimizations are similar. Both protocols enhance spectral features of the desired fast (compare Figure 2c and e) and slow (compare Figure 2d and f) pathways. The corresponding cross peaks in the 2D CI signals highlighted by red circles and green squares are optimized. It is possible to resolve new cross peaks that are due to the optimized pathways. The collinear protocol shows a smaller contrast of the peaks. For example, cross peak (5,2) due to the fast pathway is not resolved in Figure 2c and is not suppressed in Figure 2d (see arrows). (7,1) in Figure 2d is broad due to an additional unsuppressed contribution of (6,1).

The optimal coefficients are given in Table 1. The main contribution to the collinear slow pathway linear combination (slow–cl) is from the imaginary part of the $T_6^{(cl)}$ tensor component. However, the fast pathway combination consists mainly of both $T_6^{(cl)}$ and $T_8^{(cl)}$. The main contribution to the noncollinear optimal linear combination of the fast pathway optimization is $T_6^{(cl)}$, as in the collinear optimal combination. There is a negligible contribution of the imaginary part of the $T_6^{(cl)}$ component to the slow pathway noncollinear optimization. This means that the noncollinear $T_7^{(ncl)}$ tensor component is optimal for the slow pathway. The collinear finds a global optimum in its own search parameter space, which has a different linear combination of tensor components. The noncollinear optimal combination involves a significant contribution of many tensor components and shows a better selectivity.

4. PROBING EXCITON POPULATION DYNAMICS BY OPTIMIZED CHIRAL 2D SIGNALS

Our optimal coefficients can be used to predict the signals at all t_2 values and to obtain a molecular response movie of energy transport in the selected pathway. This strategy can be realized experimentally in the following steps. First, the nine linearly independent CI tensor components should be measured separately at the chosen t_2 delay times under identical experimental conditions using appropriate collinear or noncollinear laser beam configurations. Second, linear combinations of these tensor components should be constructed and optimized for a particular control target. These may be used to follow the dynamics of the desired processes.
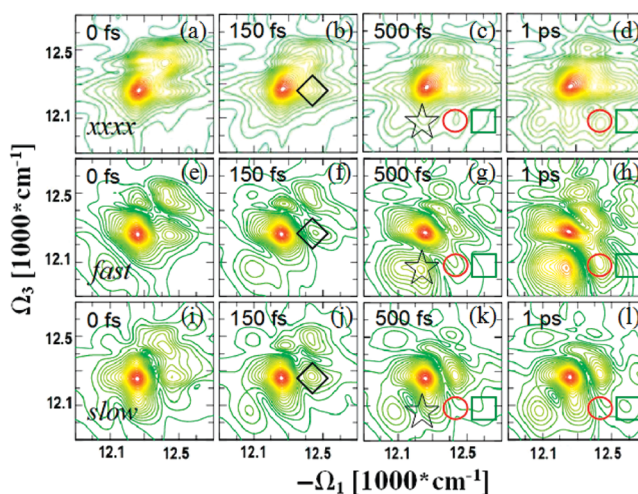

Figure 3. Variation of 2D spectra of FMO with waiting times of $t_2 = 0$, 150, and 500 fs and 1 ps. (a–d) Nonchiral *xxxx* signals. Other rows give the noncollinear coherently controlled CI linear combinations optimized for the fast (e–h) and slow (i–l) energy-transfer pathways (absolute values). Diamonds mark the cross peak (5,2). Stars mark the cross peak (2,1). Red circles and green squares mark cross peaks due to the fast and slow energy-transfer pathways, respectively.

We have applied this to our two pathways. Sequences of the 2D spectra (absolute values) for $t_2 = 0$, 150, and 500 fs and 1 ps are shown in Figure 3 top (*xxxx*), middle (fast–ncl), and bottom (slow–ncl) rows. *xxxx* is a nonchiral technique which contains spectral features from both pathways. Advanced theoretical modeling and additional data from other experiments will be necessary to assign the spectral peaks and separate different pathways. Coherent control makes it possible to eliminate spectral features that do not contribute to a selected cross peak and separate contributions of different processes. The fast–ncl and slow–ncl 2D spectra in Figure 3 (middle and bottom rows) correspond to noncollinear optimizations of the fast and slow energy-transfer pathways in FMO, respectively. CI tensor components reveal new peaks, whereas coherent control highlights spectral features of a particular pathway. Using the optimal linear combinations, it is now possible to follow the fast or slow energy-transfer pathway as a function of the t_2 waiting time.

At $t_2 = 0$ fs, all 2D spectra (Figure 3a, e, and i) look similar. Broad-band excitation covers the entire exciton manifold, and a coherent superposition of all 7 single-exciton states is excited. At $t_2 = 0$ fs, a previously unresolved diagonal peak from exciton 7 is now resolved due to chirality in the slow pathway optimization in Figure 3i. This peak is absent in the fast pathway optimization because exciton 7 does not contribute and is therefore eliminated. This diagonal peak rapidly decays with t_2 due to the energy transfer to the lower exciton states.

The cross peaks are initially weak and grow with t_2. The diamonds in Figure 3b, f, and j indicate the positions of cross peak (5,2), which belongs to the fast pathway. This peak undergoes a dynamical shape evolution with the increasing waiting time t_2 in the fast pathway optimization plots in Figure 3e–h and is correlated with cross peak (5,1) due to the energy transfer from exciton 5 to 2 and to 1. The (5,2) peak does not evolve significantly in the slow pathway optimization in Figure 3i–l and does not transfer its amplitude to (5,1). (5,1), not resolved in

xxxx (red circle in Figure 3c), is successfully enhanced and suppressed in the fast and slow optimizations, as shown in Figure 3g and k, respectively. (5,1) is totally suppressed in the slow pathway optimization (red circles in Figure 3k and l). However, in the fast pathway optimization in Figure 3g and h, this peak is enhanced and indicates an efficient energy transfer through the fast pathway (highlighted by red circles). Cross peak (7,1) shows the opposite behavior and is also successfully optimized. Cross peak (2,1) is better resolved and enhanced in Figure 3g compared to that in Figure 3c (highlighted by a star symbol). It is suppressed in Figure 3k in the optimized slow pathway and shifted to a position of the cross peak (3,1), which is due to that pathway.

5. DISCUSSION

Coherent control determined by a linear combination of CI nonlinear optical tensor components simplifies multidimensional spectra and allows one to resolve new spectral features of the molecular response of photosynthetic complexes. Optimal 2D electronic spectra of the FMO complex from photosynthetic green sulfur bacterium *Chlorobium tepidum* were designed. Better resolution is achieved compared to the nonchiral *xxxx* signals. The optimal spectra have fewer cross peaks and more clearly reveal the energy-transport mechanisms.

Cross peaks associated with the two energy-transfer pathways in FMO were selected and optimized using a genetic algorithm. The full energy-transfer dynamics was subsequently observed by constructing an optimal linear combination at various t_2 delay times. Dynamics of all exciton levels were monitored through the optimized cross peaks in the multidimensional spectra. Coherent control tools were used to generate microscopic response movies that reveal a step-by-step energy-transport process.

Noncollinear signals show a better control, narrower peaks, and improved resolution over energy-transfer pathways in FMO compared to the collinear counterparts. Table 1 shows that most tensor components have nonnegligible optimal coefficients, and therefore, taking a superposition of all nine CI tensor components is necessary to improve controllability. The difference between the collinear and the noncollinear techniques is the number of tensor components used in a linear superposition. While in the noncollinear case all nine linearly independent components are used and therefore all of the information about the system response is available, this is not the case in the collinear configuration. In the latter, only the three collinear CI tensor components are used. The success of an optimization will depend on a selected problem. In the current case, both collinear and noncollinear configurations achieve peak enhancement of the selected energy-transfer pathways in the FMO complex. This allows observation of exciton dynamics one energy-transfer pathway at a time. The collinear configuration is simpler and may serve as a first step toward coherently controlled CI multidimensional spectroscopy in the future. Laser pulse shaping techniques may be used to design more complex optimal pulse sequences.[39]

The present protocol may be applied to other natural and artificial light-harvesting systems such as more complex light-harvesting antennae in plants. The simulated optimal coefficients may be used to combine experimental data and generating optimal multidimensional signals to reveal desired targets. Knowledge of the Hamiltonian is not necessary to separate energy-transfer pathways and probe the system dynamics.

■ AUTHOR INFORMATION

Present Addresses
‡Institute for Quantum Science and Engineering, Texas A&M University, College Station, Texas.

■ AUTHOR INFORMATION

§State Key Laboratory of Supramolecular Structure and Materials, Jilin University, PR China and Physics Department, Vilnius University, Lithuania.

■ REFERENCES

(1) Mukamel, S. *Annu. Rev. Phys. Chem.* **2000**, *51*, 691.

(2) Jonas, D. M. *Annu. Rev. Phys. Chem.* **2003**, *54*, 425.

(3) Mukamel, S. *Principles of Nonlinear Optical Spectroscopy*; Oxford University Press: New York, 1995.

(4) Mukamel, S.; Abramavicius, D.; Yang, L.; Zhuang, W.; Schweigert, I. V.; Voronine, D. V. *Acc. Chem. Res.* **2009**, *42*, 553.

(5) Cho, M. *Chem. Rev.* **2008**, *108*, 1331.

(6) Abramavicius, D.; Palmieri, B.; Voronine, D. V.; Sanda, F.; Mukamel, S. *Chem. Rev.* **2009**, *109*, 2350.

(7) Ernst, R. R.; Bodenhausen, G.; , Wokaun, A. *Principles of Nuclear Magnetic Resonance in One and Two Dimensions*; Clarendon: Oxford, U.K., 1987.

(8) Vandersypen, L. M. K.; Chuang, I. L. *Rev. Mod. Phys.* **2004**, *76*, 1037.

(9) Engel, G. S.; Calhoun, T. R.; Read, E. L.; Ahn, T.-K.; Mancal, T.; Cheng, Y.-C.; Blankenship, R.; Fleming, G. *Nature* **2007**, *446*, 782.

(10) Panitchayangkoon, G.; Hayes, D.; Fransted, K. A.; Caram, J. R.; Harel, E.; Wen, J.; Blankenship, R. E.; Engel, G. S. *Proc. Natl. Acad. Sci. U.S.A.* **2010**, *107*, 12766.

(11) Collini, E.; Wong, C. Y.; Wylk, K. E.; Curmi, P. M. G.; Brumer, P.; Scholes, G. D. *Nature* **2010**, *463*, 644.

(12) Abramavicius, D.; Mukamel, S. *J. Chem. Phys.* **2010**, *133*, 064510.

(13) Abramavicius, D.; Mukamel, S. *J. Chem. Phys.* **2005**, *122*, 134305.

(14) Abramavicius, D.; Zhuang, W.; Mukamel, S. *J. Phys. B* **2006**, *39*, 5051.

(15) Abramavicius, D.; Mukamel, S. *J. Chem. Phys.* **2006**, *124*, 034113.

(16) Voronine, D.; Abramavicius, D.; Mukamel, S. *J. Chem. Phys.* **2006**, *125*, 224504.

(17) Choi, J.-H.; Cheon, S.; Lee, H.; Cho, M. *Phys. Chem. Chem. Phys.* **2008**, *10*, 3839.

(18) Abramavicius, D.; Voronine, D. V.; Mukamel, S. *Biophys. J.* **2008**, *94*, 3613.

(19) Voronine, D. V.; Abramavicius, D.; Mukamel, S. *Biophys. J.* **2008**, *95*, 4896.

(20) Abramavicius, D.; Mukamel, S. *J. Chem. Phys.* **2004**, *120*, 8373.

(21) Voronine, D.; Abramavicius, D.; Mukamel, S. *J. Chem. Phys.* **2006**, *124*, 034104.

(22) Voronine, D.; Abramavicius, D.; Mukamel, S. *J. Chem. Phys.* **2007**, *126*, 044508.

(23) Prokhorenko, V. I.; Halpin, A.; Miller, R. J. D. *Opt. Exp.* **2009**, *17*, 9764.

4628

dx.doi.org/10.1021/jp111555h |*J. Phys. Chem. A* 2011, 115, 4624–4629

(24) Rice, S.; Zhao, M. *Optical Control of Molecular Dynamics*; Wiley: New York, 2000.

(25) Shapiro, M.; Brumer, P. *Principles of the Quantum Control of Molecular Processes*; John Wiley and Sons: Hoboken, NJ, 2003.

(26) Herek, J. L.; Wohlleben, W.; Cogdell, R. J.; Zeidler, D.; Motzkus, M. *Nature* **2002**, *417*, 533.

(27) Savolainen, J.; Fanciulli, R.; Dijkhuizen, N.; Moore, A. L.; Hauer, J.; Backup, T.; Motzkus, M. *Proc. Natl. Acad. Sci. U.S.A.* **2008**, *105*, 7641.

(28) Read, E. L.; Engel, G. S.; Calhoun, T. R.; Mancal, T.; Ahn, T. K.; Blankenship, R. E.; Fleming, G. R. *Proc. Natl. Acad. Sci. U.S.A.* **2007**, *104*, 14203.

(29) Read, E. L.; Schlau-Cohen, G. S.; Engel, G. S.; Wen, J.; Blankenship, R. E.; Fleming, G. R. *Biophys. J.* **2008**, *95*, 847.

(30) Renger, T. *Biophys. J.* **2008**, *95*, 495.

(31) Hochstrasser, R. M. *Chem. Phys.* **2001**, *266*, 273.

(32) Zanni, M. T.; Ge, N.-H.; Kim, Y. S.; Hochstrasser, R. M. *Proc. Natl. Acad. Sci. U.S.A.* **2001**, *98*, 11265.

(33) Zhuang, W.; Abramavicius, D.; Voronine, D. V.; Mukamel, S. *Proc. Natl. Acad. Sci. U.S.A.* **2007**, *104*, 14233.

(34) Voronine, D. V.; Abramavicius, D.; Mukamel, S. *Ultrafast Phenomena XVI*; Springer Series in Chemical Physics; 2009; Vol. 92.

(35) Brixner, T.; Stenger, J.; Vaswani, H.; Cho, M.; Blankenship, R.; Fleming, G. *Nature* **2005**, *434*, 625.

(36) Goldberg, D. E., *Genetic Algorithms in Search, Optimization, and Machine Learning*; Addison-Wesley: Reading, MA, 1989.

(37) Olson, J. M. *Photosynth. Res.* **2004**, *80*, 181.

(38) Cho, M.; Vaswani, H. M.; Brixner, T.; Stenger, J.; Fleming, G. R. *J. Phys. Chem. B* **2005**, *109*, 10542.

(39) Vaughan, J. C.; Hornung, T.; Stone, K. W.; Nelson, K. A. *J. Phys. Chem. B* **2007**, *111*, 4873.